High-resolution, low-dose phase contrast X-ray tomography for 3D diagnosis of human breast cancers

Yunzhe Zhao[a,1], Emmanuel Brun[b,c,1], Paola Coan[c,d], Zhifeng Huang[a], Aniko Sztrókay[d], Paul Claude Diemoz[c], Susanne Liebhardt[d], Alberto Mittone[c], Sergei Gasilov[c], Jianwei Miao[a,2], and Alberto Bravin[b,2]

[a]Department of Physics and Astronomy and California NanoSystems Institute, University of California, Los Angeles, CA 90095; [b]European Synchrotron Radiation Facility, 38043 Grenoble Cedex, France; [c]Faculty of Physics, Ludwig Maximilians University, 85748 Garching, Germany; and [d]Department of Clinical Radiology, Ludwig Maximilians University, 81377 Munich, Germany

Edited by Joe W. Gray, Oregon Health and Science University, Portland, OR, and accepted by the Editorial Board September 19, 2012 (received for review March 16, 2012)

Mammography is the primary imaging tool for screening and diagnosis of human breast cancers, but ∼10–20% of palpable tumors are not detectable on mammograms and only about 40% of biopsied lesions are malignant. Here we report a high-resolution, low-dose phase contrast X-ray tomographic method for 3D diagnosis of human breast cancers. By combining phase contrast X-ray imaging with an image reconstruction method known as equally sloped tomography, we imaged a human breast in three dimensions and identified a malignant cancer with a pixel size of 92 μm and a radiation dose less than that of dual-view mammography. According to a blind evaluation by five independent radiologists, our method can reduce the radiation dose and acquisition time by ∼74% relative to conventional phase contrast X-ray tomography, while maintaining high image resolution and image contrast. These results demonstrate that high-resolution 3D diagnostic imaging of human breast cancers can, in principle, be performed at clinical compatible doses.

radiation dose reduction | iterative algorithm | analyzer based imaging

Mammography is a widely used imaging technique for early detection of human breast cancers. Although more advanced technologies such as digital mammography have been developed to improve its image quality (1), there are three potential risks associated with mammography. First, mammograms miss up to 20% of breast cancers that are present during the time of screening (2). Second, in some cases mammograms appear abnormal, but no breast cancers are actually present (3). Third, repeated mammography examinations have the potential of causing cancers (4). Dedicated breast computed tomography (CT) can reduce some of these risks, but its spatial resolution (∼400 μm) is mainly limited by the X-ray dose deliverable to the radiation-sensitive human breast and its detection of microcalcifications is inferior to mammography (5). Furthermore, some tumors are not visible in CT because its image contrast is based on the X-ray absorption coefficient and is intrinsically low between tumors and normal tissues. A very promising approach to significantly improve the image resolution, image contrast and detectability is the use of phase contrast x-ray tomography (PCT) (6–8) (*Materials and Methods*). Compared with absorption-based CT, PCT is sensitive to the refraction (i.e., "phase shift") of X-rays in matter. In soft tissues, phase variations can be two to three orders of magnitude larger than the absorption ones (9), and thus an increased image contrast can be achieved. Over the past few decades, phase contrast X-ray imaging has been under rapid development and various X-ray phase contrast methods have been implemented, including X-ray interferometry (6, 7), analyzer-based (or diffraction-enhanced) imaging (10, 11), propagation-based imaging (12, 13), grating-based imaging (14, 15), and grating noninterferometric methods (16). A large number of X-ray phase contrast imaging results has been reported on both technical developments and biomedical applications (6–20). In vitro and in vivo biomedical studies have focused on demonstrating high diagnostic significance of PCI images in a wide range of pathologies related to breast (8), joint and cartilage (17), lung (18), and central nervous system (19). Clinical trials have also been performed in PCI mammography (20). Furthermore, the development of advanced optics for the use of 50–80 keV (instead of 15–30 keV) X-rays has dramatically increased the sample size under study in PCT (8, 17). However, presently two of the major challenges prevent PCT from becoming an in vivo imaging tool for clinical application. First, to achieve high resolutions (i.e., tens of microns) for accurate diagnosis, PCT requires several thousands of projections from a whole human breast. The total radiation dose delivered to the breast is thus higher than that in dual-view mammography. Second, PCT uses sophisticated X-ray optics and the acquisition time for several thousands of projections is usually too long for clinical application.

In this article, we demonstrate a high-resolution, high-contrast, and low-dose PCT method for 3D imaging of a whole human breast sample with an invasive ductal cancer. We chose an invasive ductal carcinoma in this study because it is the most frequent breast cancer entity (>70% of all breast malignancies). By combining PCT with a data acquisition and reconstruction method, termed equally sloped tomography (EST, *Materials and Methods*) (21–25), we imaged a human breast cancer sample in three dimensions with a pixel size of 92 μm. Compared with the conventional PCT method, our approach enables reduction of the radiation dose and acquisition time by ∼74% without compromising the resolution, image contrast and image quality. Thus, this work represents an important experimental step toward clinical application of PCT for 3D diagnostic imaging of human breast cancers.

The experiment was conducted on the biomedical beamline at the European Synchrotron Radiation Facility (ESRF) (26). The sample was a human breast mastectomy specimen (∼9.5 cm in diameter) issued from a 75-y-old woman with an invasive ductal cancer and fixed in 4% formalin. The study was conducted in accordance with the Declaration of Helsinki and was approved by the local ethics committee. A monochromatic and collimated X-ray beam with energy of 60 keV was used to image the breast cancer sample (Fig. 1). The use of 60-keV X-rays was to reduce the radiation dose to the sample and allowed for the imaging of thick tissues. The refracted and scattered X-rays by the sample were analyzed by a perfect silicon crystal. The analyzer acts as an extremely narrow slit which selects X-rays exiting the sample with

Author contributions: P.C., J.M., and A.B. designed research; Y.Z., E.B., P.C., A.S., P.C.D., A.M., S.G., J.M., and A.B. performed research; Y.Z., E.B., Z.H., A.S., P.C.D., S.L., and J.M. analyzed data; and Y.Z., E.B., P.C., J.M., and A.B. wrote the paper.

The authors declare no conflict of interest.

This article is a PNAS Direct Submission. J.W.G. is a guest editor invited by the Editorial Board.

[1]Y.Z. and E.B. contributed equally to this work.

[2]To whom correspondence may be addressed. E-mail: miao@physics.ucla.edu or bravin@esrf.fr.

This article contains supporting information online at www.pnas.org/lookup/suppl/doi:10.1073/pnas.1204460109/-/DCSupplemental.

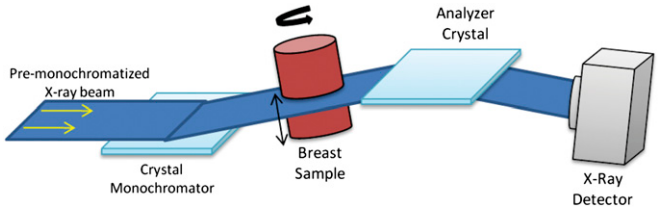

Fig. 1. Schematic diagram of the phase contrast X-ray imaging set-up. A collimated X-ray beam with energy of 60 keV was monochromatized by a double Si (111) crystal system and an additional single Si (333) crystal. The breast cancer sample was mounted on a rotary stage and positioned in the X-ray beam. The refracted and scattered X-rays by the sample were analyzed by a Si (333) analyzer crystal. The analyzer crystal was rotated according to the incoming X-ray beam and set at an angle close to the Bragg diffraction condition. After each rotation, the sample was vertically displaced relative to the X-ray beam, allowing a different region to be imaged. A fast-readout and low-noise charge-coupled device (CCD) camera with 2,048 × 2,048 pixels was used to measure the phase contrast X-ray images.

extremely high sensitivity (~10^{-6} radian). A fast readout and low noise charge coupled device (CCD) camera with 2,048 × 2,048 pixels was mounted after the analyzer (27). The effective pixel size of the CCD after a 2 × 2 binning was 92 × 92 μm^2, which sets the spatial resolution of the imaging technique.

To achieve high spatial resolution in conventional PCT, the number of projections (N) required is determined by $N \sim \pi D/(2P)$, where D is the thickness of the sample and P the detector pixel size. In this experiment, 2,000 projections were measured from the whole breast cancer sample. Although the acquired projections are a mixture of the X-ray absorption, refraction, and scatter effects, the application of CT reconstruction methods remains valid due to the small refraction angle approximation for soft tissues (28). The 3D structure of the breast cancer sample was reconstructed with the EST method, which iterates back and forth between real and Fourier space by using the pseudopolar fast Fourier transform (Fig. 2, *Materials and Methods*, and Fig. S1) (21–25). In each iteration, physical constraints including the sample boundary and the positivity of the sample structure are enforced in real space, whereas the Fourier transform of the measured projections are imposed in Fourier space. The algorithm, monitored by an error metric, is guided toward a solution that is consistent with the measured data. To prevent any human intervention, the algorithm is automatically terminated when no further improvement can be made. Compared with coherent diffraction imaging in which an iterative algorithm is used to retrieve the phase information from oversampled diffraction intensities (29), EST uses an iterative algorithm to reconstruct a best-possible image that is consistent with the Fourier transform of the measured projections as well as the physical constraints in real space (21–25). After the iteration process was finished, a nonlocal means technique was applied to the reconstructed image (30). This technique has proven to be effective in removing noise while preserving edge contrast. In our case, the nonlocal means filter was carefully selected to partially eliminate noise but not fine structures.

Results

Image Quality Comparison Between the Conventional PCT and EST Reconstructions. We performed a conventional PCT reconstruction of the whole breast cancer sample from 2,000 projections using the gold-standard filtered back projection (FBP) with a Hamming filter (31). The same volume was computed with an EST reconstruction using 512 of the 2,000 projections. For a comparison purpose, a FBP reconstruction was also computed with 512 projections. To explore the limit of the EST method and investigate the possibility of further reducing the radiation dose and the acquisition time, we also performed an EST reconstruction with only 200 projections. Fig. 3 *A–E* and Fig. S2 show three sagittal and axial slices of the FBP 2000, EST 512, FBP 512, and EST 200 reconstructions. A zoomed view of the breast tumor region is shown in Fig. 3 *B–E* and Fig. S2 *E–H*. Visually, the EST 512 reconstruction looks very consistent with FBP 2000, whereas FBP 512 exhibits high noise, degraded features (arrows), and blurred boundary of the tumor.

For each of the four reconstructions (FBP 2000, EST 512, FBP 512, and EST 200), two sets of images (an axial slice and a sagittal slice) were selected and blindly examined by five experienced radiologists. The different tumor borders, skin layers, fatty tissues, and collagen strands were easily identified by the radiologists. To make the evaluation quantitative, five criteria were adopted by the radiologists based on current clinical image evaluation systems (32). The criteria include (*i*) overall image quality, (*ii*) image sharpness, (*iii*) image contrast (*iv*) evaluation of different structure, and (*v*) noise level. They were evaluated in a range from 1 to 5 (1 being the worst and 5 the best). Table 1 summarizes the results of the blind evaluation, suggesting that EST 512 even slightly outperforms FBP 2000 in all five categories. Furthermore, the EST 200 reconstruction is not only superior to FBP 512, but also shows an image quality with fine structures that is still clinically acceptable.

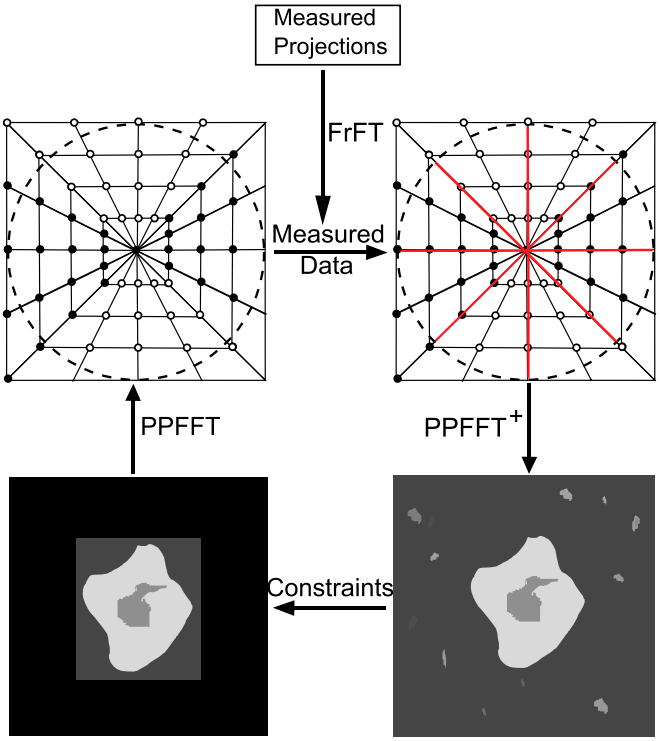

Fig. 2. Schematic layout of the iterative EST algorithm. The algorithm starts with padding each projection with zeros and calculating its oversampled Fourier slice in the pseudopolar grid (red lines; *Upper Right*) using the fractional Fourier transform (FrFT) (44). By applying the adjoint PPFFT to the Fourier-space slices (24), a real-space image is obtained (*Lower Right*), from which a support is determined. The voxel values outside the support are set to zero to obtain a new image (*Lower Left*). By applying the PPFFT to the new image, an updated set of Fourier-space slices is obtained (*Upper Left*). Those Fourier slices corresponding to red lines in *Upper Right* are replaced with the measured ones, whereas the grid points outside the resolution circle and on the missing Fourier slices (black lines in *Upper Right*) remain unchanged. The updated Fourier slices are used for the next iteration. The algorithm is monitored by an error metric, defined as normalized difference between the measured and calculated Fourier slices, and is automatically terminated when no further improvement can be made.

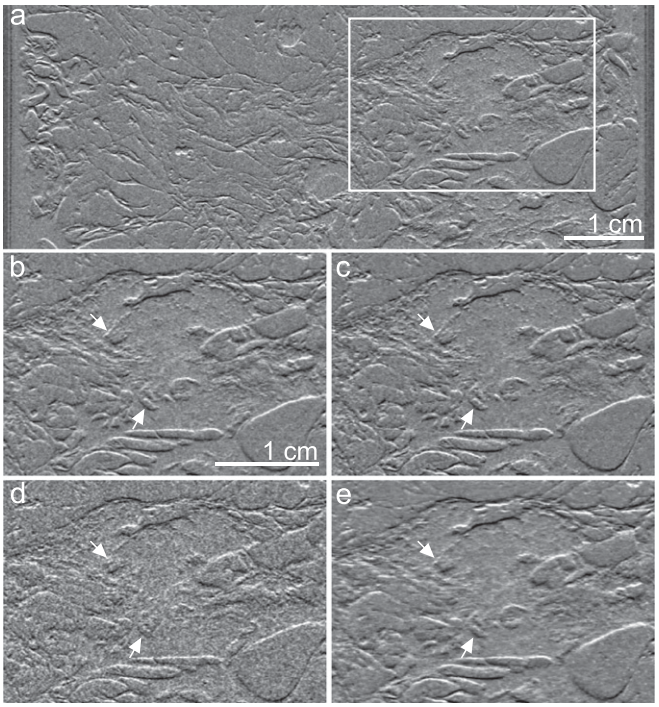

Fig. 3. Image quality comparison between the conventional PCT and EST reconstructions. (*A*) A 92-μm-thick sagittal slice of the FBP 2000 reconstruction, in which the rectangle indicates a tumor region. (*B*–*E*) Zoomed view of the tumor region reconstructed by FBP 2000 (*B*), EST 512 (*C*), FBP 512 (*D*), and EST 200 (*E*). The arrows indicate that FBP 2000 and EST 512 have the highest image quality, whereas FBP 512 exhibits high noise, degraded features, and blurred boundary of the tumor. A Hamming filter was used in the FBP reconstructions, whereas a nonlocal means filter was applied to the EST reconstructions.

A reformatted 92-μm-thick sagittal slice (which was used for the evaluation) and an axial slice from the EST 512 reconstruction are shown in Fig. 4. The fine details of the tumor, collagen strands, glandular tissue, and fat are clearly resolved. Fig. 4 *B* and *D* shows a zoomed view of the tumor region, in which the border of the tumor is distinctly visible and exhibits sharp edges. The partially discreet spiculations are a sign of malignancy in mammography. The tissue segmentation on the EST 512 reconstruction has been performed using a segmentation method based on 3D marker-controlled viscous watershed transform (33). This method is well adapted for the intrinsic nature of the PCT images, which are characterized by a strong signal at the borders of each feature. Fig. 5*A* shows the segmented tumor in an axial slice, in which the yellow contour line indicates the tumor boundary. Three perpendicular slices of the segmentation are shown in Fig. 5*B*, and the whole 3D volume renderings are displayed in Fig. 5*C* and Movie S1. The 3D segmented tumor (in red) and its surrounding tissues such as skin, lobules, and lactiferous duct are clearly visible, and the total volume of the elongated tumor was estimated to be ~2.7 cm^3. These results, along with the radiologists' evaluation, demonstrate that the EST method not only significantly reduces the number of projections relative to the standard FBP method, but also preserves the high resolution and sensitivity of PCT in discriminating the fine 3D structures and morphology of the tumor and soft tissues. To further quantify the EST and FBP reconstructions under the same condition, we applied a nonlocal means filter to both the EST 512 and FBP 512 reconstructions. Fig. S3 shows a 92-μm-thick sagittal slice and the zoomed view of the tumor region, suggesting that the improvement of the image resolution and contrast is mainly due to the EST method.

Table 1. Results of a blind evaluation made by five independent, experienced radiologists

	FBP 2000	EST 512	FBP 512	EST 200
Overall image quality	4.3 ± 0.9	4.5 ± 0.5	2.2 ± 0.4	2.7 ± 0.9
Sharpness	4.0 ± 0.7	4.3 ± 0.5	3.3 ± 0.5	2.2 ± 0.8
Image contrast	4.0 ± 0.5	4.8 ± 0.4	3.0 ± 0.7	3.4 ± 1.0
Evaluation of different structure	4.1 ± 0.6	4.8 ± 0.4	2.6 ± 0.5	2.9 ± 1.0
Noise level	4.2 ± 0.6	4.8 ± 0.3	1.8 ± 0.8	3.3 ± 0.8

Two sets of images each consisting of the FBP 2000, EST 512, FBP 512, and EST 200 reconstructions were used in the evaluation based on five criteria: overall image quality, image sharpness, image contrast, evaluation of different structure, and noise level, where "5" means the best and "1" the worst. A Hamming filter was used in the FBP reconstructions, whereas a nonlocal means filter was applied to the EST reconstructions.

Radiation Dose Estimation in the Conventional PCT and EST Reconstructions. The radiation dose for the FBP 2000 and EST 512 reconstructions was estimated based on the measurement using an ionization chamber installed on the biomedical beamline. The Mean Glandular Dose (MGD), calculated by Monte Carlo simulations (34), is 7.7 ± 0.1 mGy for the FBP 2000 reconstruction and 2.0 ± 0.1 mGy for the EST 512 reconstruction, suggesting that EST allows for a radiation dose reduction of ~74% relative to the conventional FBP reconstruction. Furthermore, according to the US Food and Drug Administration (FDA), the MGD of the US dual-view screening mammography system was estimated to be ~3.0–3.52 mGy (35). Therefore, the combination of EST and PCT cannot only provide high-resolution and high-contrast 3D diagnosis of human breast cancers, but also requires radiation doses less than that in dual-view screening mammography. According to the blind evaluation by five radiologists, although the overall image quality is lower than that of EST 512 and FBP 2000, EST 200 still outperforms FBP 512, and the 3D breast tumor structure remains visible. The total radiation dose in EST 200 is reduced to 0.8 ± 0.1 mGy, which is about four times lower than that in dual-view screening mammography.

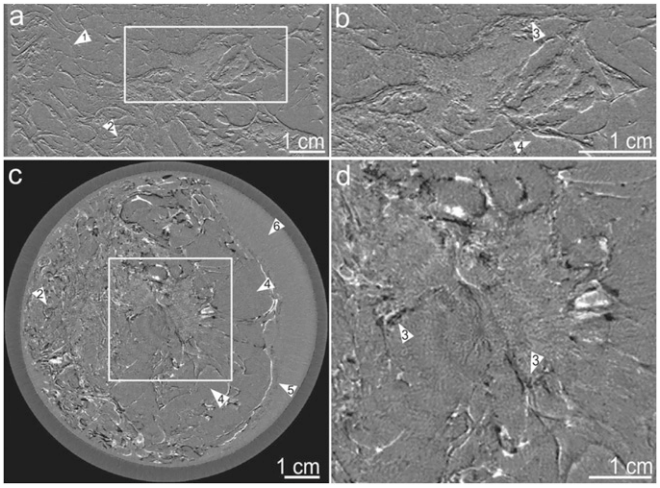

Fig. 4. Identification of fine features in the tumor region and its surrounding tissues in the EST 512 reconstruction. (*A*) A 92-μm-thick sagittal slice (the rectangle indicates the tumor region). (*B*) Zoomed view of the tumor region in the sagittal slice. (*C*) A 92-μm-thick axial slice (the square indicates the tumor region). (*D*) Zoomed view of the tumor region in the axial slice. The arrows indicate various fine features in the EST 512 reconstruction: 1, collagen strands; 2, glandular tissue; 3, spiculations; 4, fat; 5, skin; and 6, formalin.

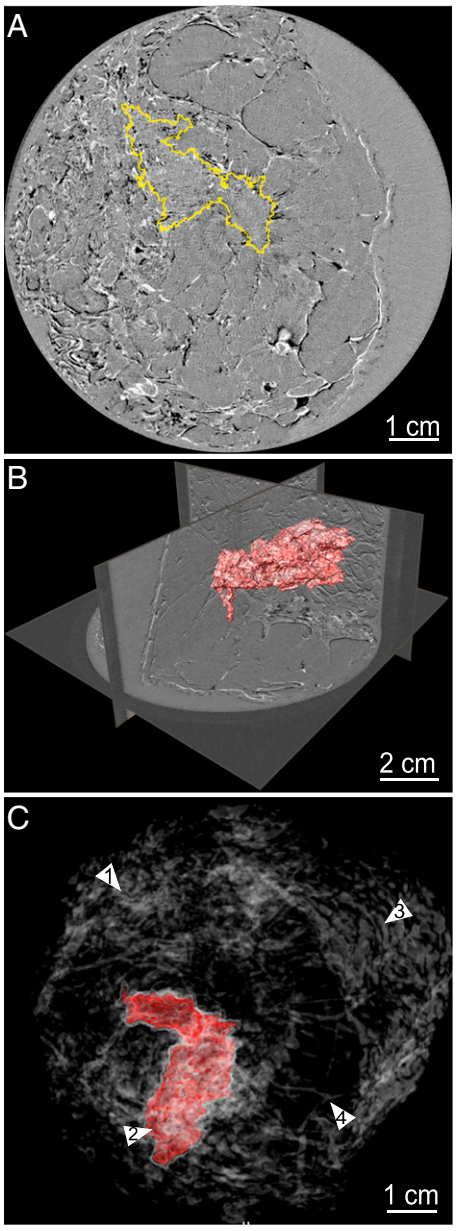

Fig. 5. Three-dimensional visualization of the tumor from the EST 512 reconstruction. (*A*) A segmented tumor in an axial slice, in which the yellow contour line indicates the tumor boundary. (*B*) Three perpendicular slices of the segmented tumor (in red). (*C*) Three-dimensional volume renderings of the tumor (in red) in which the arrows indicate different fine features: 1, lobules; 2, tumor; 3, skin; and 4, lactiferous duct.

Discussion and Conclusion

Compared with the conventional FBP based PCT method, the EST approach uses an iterative process to search for the missing information from a limited number of projections, while keeping the reconstruction consistent with the experimental data and physical constraints. Furthermore, the EST method implemented in this study requires no interpolation in Fourier space, and is automatically terminated when a solution is reached. Because of the use of a fast Fourier transform in the iterative process, the computational time for a 2,048 × 2,048 pixel slice with 21 EST iterations is about 1.4 min on a 2.66 GHz Intel Nehalem computer with 4 GB of RAM. By combining this general reconstruction method with PCT, we not only achieved high-contrast 3D imaging of a human breast cancer sample with a pixel size of 92 μm, but also reduced the radiation dose by ~74% relative to the standard PCT method. As importantly, the significant reduction of the number of projections also implies that the acquisition time can in principle be improved by a factor of ~74% (i.e., reduced from 25.1 to 6.6 min), which is another critical factor in pursuing in vivo imaging and clinical application of PCT. Furthermore, if a slightly higher noise level is tolerable, the EST method may be applied to the screening and diagnosis of human breast cancers with an even lower radiation dose (~0.8 ± 0.1 mGy) and a faster acquisition time (~2.5 min).

In conclusion, we have demonstrated that, compared with current clinical mammography, the EST based PCT method cannot only provide the 3D information of soft tissues and tumors at higher resolution and better contrast, but also deliver less radiation doses to the sample. An important step toward the clinical implementation of this method is the requirement of compact X-ray sources that enable to deliver quasi monochromatic X-rays with flux densities between those available at the large scale synchrotron radiation and at the clinical X-ray generators. Fortunately, such compact X-ray sources are currently under rapid development worldwide, including compact synchrotron radiation (36, 37), tabletop high harmonic generation (38), Compton backscattering systems (39), and liquid-metal-jet-anode microfocus sources (40). Finally, although we used a human breast cancer sample as proof of principle in this study, this method can in principle be applied to other medical tomography fields where high resolution, high contrast, low radiation doses and fast data acquisition are crucially needed.

Materials and Methods

Phase Contrast Imaging Technique. The behavior of X-rays as they travel through an object can be described in terms of a complex index of refraction, of which the real part (δ) represents the phase shift (refraction) and the imaginary part (β) represents X-ray absorption by the object. In conventional radiography, the image contrast is generated by X-ray absorption that arises from the difference of the density and the change in the sample thickness and composition. The variation of the linear attenuation coefficients for biological soft tissues is typically on the order of 0.1–0.3 cm^{-1} in the X-ray energy range of 10–60 keV (41), which is commonly used in radiology. As a result, the image contrast based on X-ray absorption may not be sufficiently high enough to image the normal and diseased tissues in a sample. Compared with X-ray absorption, the phase shift in the hard X-ray energy range is two to three orders of magnitude higher (10). Therefore, radiographic techniques that are sensitive to the variation of the phase shift can significantly enhance the image contrast relative to the X-ray absorption based techniques.

In this experiment, a collimated X-ray beam with energy of 60 keV was monochromatized by a double Si (111) crystal system and an additional single Si (333) crystal (Fig. 1). The breast cancer sample was mounted on a rotary stage and placed in the X-ray beam. The refracted and scattered X-rays by the sample were analyzed by a Si (333) analyzer crystal. The analyzer crystal was rotated according to the incoming X-ray beam and set at an angle close to the Bragg diffraction condition. After each rotation, the sample was vertically displaced relative to the X-ray beam, allowing a different region to be imaged. A 60-μm-thick Gadox fluorescent screen was used to convert the X-rays into visible light and was then recorded by the 2,048 × 2,048 pixel CCD camera (27). The images were taken with a 2 × 2 binning to have a 92 μm pixel size for a total acquisition time of ~25.1 min.

The image contrast of this experimental set-up is determined by the rocking curve of the analyzer crystal. The analyzer modulates the beam by converting the small angular change of the X-ray propagation to the intensity variation on the detector. Depending on the position of the analyzer crystal, the image contrast varies because the Bragg condition is fulfilled by the refracted and scattered X-rays at different angles from the sample. In this study, we set the position of the analyzer about 40% to the left of the rocking curve peak.

Iterative EST Algorithm. Unlike conventional CT reconstruction methods, EST uses a pseudopolar grid and the pseudopolar fast Fourier transform (PPFFT) (42). Fig. S1 shows the geometrical relationship between a pseudopolar grid, a Cartesian grid and the PPFFT. For an $N \times N$ Cartesian grid, the corresponding pseudopolar grid is defined by a set of 2N lines, each line consisting of 2*N* grid points mapped out on *N* concentric squares. The pseudopolar lines are termed

"equally sloped" because the slope of each successive line changes by an equal slope increment as opposed to a fixed equal angular increment in the polar grid. The pseudopolar grid is related to its corresponding Cartesian grid by the PPFFT. To use this special geometry for tomographic reconstructions, the algorithm starts with padding each projection with zeros and calculating its oversampled Fourier slice in the pseudopolar grid (red lines in Fig. 2 *Upper Right*). The oversampling concept (i.e., sampling the Fourier slice at a frequency finer than the Nyquist interval) has been widely used to solve the phase problem in coherent diffraction imaging (29, 43). In the EST method, oversampling does not provide extra information about the object, but allows the use of iterative algorithms to retrieve the missing data from the measured projections and physical constraints. The grid points outside the resolution circle (the circle with dashed lines in Fig. 2) and on the missing projections (black lines in Fig. 2 *Upper Right*) are set to zero. The algorithm iterates back and forth between real and Fourier space by the following steps (21–25):

i) A real-space image is obtained (Fig. 2 *Lower Right*) by applying the adjoint PPFFT to the Fourier-space slices. Here the adjoint PPFFT instead of the inverse PPFFT is used because the former is implemented by avoiding the conjugate gradient method and can be computed faster than the latter without compromising the accuracy (24).

ii) A support is determined from the image based on the zero padding of the projections. Outside the support the voxel values are set to zero, and inside the support the negative values are set to zero. A new image is obtained (Fig. 2 *Lower Left*).

iii) By applying the PPFFT to the new image, an updated set of Fourier-space slices is obtained (Fig. 2 *Upper Left*).

iv) Those Fourier slices corresponding to red lines in Fig. 2 are replaced with the measured ones, whereas the grid points outside the resolution circle and on the missing Fourier slices (i.e., black lines) remained unchanged. The revised set of the Fourier slices is used for the next iteration.

v) An error metric is calculated to monitor the convergence of the algorithm, defined as normalized difference between the measured and calculated Fourier slices.

In this experiment, the algorithm was automatically terminated when the error became stabilized after about 20 iterations.

ACKNOWLEDGMENTS. We thank the ESRF for providing the experimental facilities, the ESRF ID17 team for assistance in operating the facilities, and radiologists K. Hellerhoff, G. Schmidt, M. Notohamiprodjo, and F. Bamberg for a blind, independent evaluation of our data (the fifth radiologist is S.L.). This work was partially supported by UC Discovery/TomoSoft Technologies Grant IT107-10166, National Institutes of Health Grant GM081409-01A1, and the DFG–Cluster of Excellence Munich–Centre for Advanced Photonics EXE158.

1. Pisano ED, et al.; Digital Mammographic Imaging Screening Trial (DMIST) Investigators Group (2005) Diagnostic performance of digital versus film mammography for breast-cancer screening. *N Engl J Med* 353(17):1773–1783.
2. Brewer NT, Salz T, Lillie SE (2007) Systematic review: The long-term effects of false-positive mammograms. *Ann Intern Med* 146(7):502–510.
3. Kolb TM, Lichy J, Newhouse JH (2002) Comparison of the performance of screening mammography, physical examination, and breast US and evaluation of factors that influence them: an analysis of 27,825 patient evaluations. *Radiology* 225(1):165–175.
4. Feig SA, Hendrick RE (1997) Radiation risk from screening mammography of women aged 40-49 years. *J Natl Cancer Inst Monogr* 22(22):119–124.
5. Lindfors KK, et al. (2008) Dedicated breast CT: Initial clinical experience. *Radiology* 246(3):725–733.
6. Momose A, Takeda T, Itai Y, Hirano K (1996) Phase-contrast X-ray computed tomography for observing biological soft tissues. *Nat Med* 2(4):473–475.
7. Takeda T, et al. (2000) Human carcinoma: Early experience with phase-contrast X-ray CT with synchrotron radiation—comparative specimen study with optical microscopy. *Radiology* 214(1):298–301.
8. Sztrókay A, et al. (2012) High-resolution breast tomography at high energy: A feasibility study of phase contrast imaging on a whole breast. *Phys Med Biol* 57(10): 2931–2942.
9. Fitzgerald R (2000) Phase-sensitive X-Ray imaging. *Phys Today* 53:23–27.
10. Davis TJ, Gao D, Gureyev TE, Stevenson AW, Wilkins SW (1995) Phase-contrast imaging of weakly absorbing materials using hard X-rays. *Nature* 373:595–598.
11. Chapman D, et al. (1997) Diffraction enhanced x-ray imaging. *Phys Med Biol* 42(11): 2015–2025.
12. Snigirev A, Snigireva I, Kohn V, Kuznetsov S, Schelokov I (1995) On the possibilities of x-ray phase contrast microimaging by coherent high-energy synchrotron radiation. *Rev Sci Instrum* 66:5486–5492.
13. Wilkins SW, Gureyev TE, Gao D, Pogany A, Stevenson AW (1996) Phase-contrast imaging using polychromatic hard X-rays. *Nature* 384:335–338.
14. Pfeiffer F, Weitkamp T, Bunk O, David C (2006) Phase retrieval and differential phase-contrast imaging with low-brilliance X-ray sources. *Nat Phys* 2:258–261.
15. Zhu P, et al. (2010) Low-dose, simple, and fast grating-based X-ray phase-contrast imaging. *Proc Natl Acad Sci USA* 107(31):13576–13581.
16. Olivo A, Diemoz PC, Bravin A (2012) Amplification of the phase contrast signal at very high x-ray energies. *Opt Lett* 37(5):915–917.
17. Li J, Zhong Z, Connor D, Mollenhauer J, Muehleman C (2009) Phase-sensitive X-ray imaging of synovial joints. *Osteoarthritis Cartilage* 17(9):1193–1196.
18. Beltran MA, et al. (2011) Interface-specific x-ray phase retrieval tomography of complex biological organs. *Phys Med Biol* 56(23):7353–7369.
19. Pinzer BR, et al. (2012) Imaging brain amyloid deposition using grating-based differential phase contrast tomography. *Neuroimage* 61(4):1336–1346.
20. Castelli E, et al. (2011) Mammography with synchrotron radiation: First clinical experience with phase-detection technique. *Radiology* 259(3):684–694.
21. Miao J, Föster F, Levi O (2005) Equally sloped tomography with oversampling reconstruction. *Phys Rev B* 72:052103.
22. Lee E, et al. (2008) Radiation dose reduction and image enhancement in biological imaging through equally-sloped tomography. *J Struct Biol* 164(2):221–227.
23. Fahimian BP, Mao Y, Cloetens P, Miao J (2010) Low-dose x-ray phase-contrast and absorption CT using equally sloped tomography. *Phys Med Biol* 55(18):5383–5400.
24. Mao Y, Fahimian BP, Osher SJ, Miao J (2010) Development and optimization of regularized tomographic reconstruction algorithms utilizing equally-sloped tomography. *IEEE Trans Image Process* 19(5):1259–1268.
25. Scott MC, et al. (2012) Electron tomography at 2.4-ångström resolution. *Nature* 483 (7390):444–447.
26. Bravin A, et al. (2007) High-resolution CT by diffraction-enhanced x-ray imaging: Mapping of breast tissue samples and comparison with their histo-pathology. *Phys Med Biol* 52(8):2197–2211.
27. Coan P, et al. (2006) Evaluation of imaging performance of a taper optics CCD 'FReLoN' camera designed for medical imaging. *J. Synch. Rad* 13:260–270.
28. Diemoz PC, Bravin A, Glaser C, Coan P (2010) Comparison of analyzer-based imaging computed tomography extraction algorithms and application to bone-cartilage imaging. *Phys Med Biol* 55(24):7663–7679.
29. Miao J, Charalambous P, Kirz J, Sayre D (1999) Extending the methodology of X-ray crystallography to allow imaging of micrometre-sized non-crystalline specimens. *Nature* 400:342–344.
30. Buades A, Coll B, Morel JM (2005) A review of image denoising algorithms with a new one. *Multiscale Model Simul.* 4:490–530.
31. Kak AC, Slaney M (2001) *Principles of Computerized Tomographic Imaging* (SIAM, Philadelphia, PA).
32. Li Y, Poulos A, McLean D, Rickard M (2010) A review of methods of clinical image quality evaluation in mammography. *Eur J Radiol* 74(3):e122–e131.
33. Vachier C, Meyer F (2005) The viscous watershed transform. *J Math Imaging Vis* 22: 251–267.
34. Strulab D, Santin G, Lazaro D, Breton V, Morel C (2003) GATE (geant4 application for tomographic emission): A PET/SPECT general-purpose simulation platform. *Nucl Phys B Proc Suppl* 125:75–79.
35. Health Center for Devices and Radiological Center National Statistics (MQSA) (2003) Dose and Image Quality in Mammography: Trends During the First Decade of MQSA. Available at http://www.fda.gov/Radiation-EmittingProducts/MammographyQualityStandardsActandProgram/FacilityScorecard/ucm113606.htm. Accessed September 30, 2012.
36. Schlenvoigt HP, et al. (2008) A compact synchrotron radiation source driven by a laser-plasma wakefield accelerator. *Nat Phys* 4:130–133.
37. Kneip S, et al. (2010) Bright spatially coherent synchrotron X-rays from a table-top source. *Nat Phys* 6:980–983.
38. Popmintchev T, et al. (2012) Bright coherent ultrahigh harmonics in the keV x-ray regime from mid-infrared femtosecond lasers. *Science* 336(6086):1287–1291.
39. Carroll FE, Mendenhall MH, Traeger RH, Brau C, Waters JW (2003) Pulsed tunable monochromatic X-ray beams from a compact source: New opportunities. *AJR Am J Roentgenol* 181(5):1197–1202.
40. Tuohimaa T, Otendal M, Hertz HM (2007) Phase contrast x-ray imaging with a liquid-metal-jet-anode microfocus source. *Appl Phys Lett* 91:074104.
41. Chantler CT, et al. (2005) X-ray form factor, attenuation and scattering tables (version 2.1). Available at http://physics.nist.gov/ffast. Accessed September 30, 2012.
42. Averbuch A, Coifman RR, Donoho DL, Israeli M, Shkolnisky Y (2008) A framework for discrete integral transformations I—the pseudopolar Fourier Transform. *SIAM J Sci Comput* 30:785–803.
43. Miao J, Sayre D, Chapman HN (1998) Phase retrieval from the magnitude of the Fourier transform of non-periodic objects. *J. Opt. Soc. Am. A. A* 15:1662–1669.
44. Bailey DH, Swarztrauber PN (1991) The fractional Fourier transform and applications. *SIAM Rev* 33:389–404.